Improved 1D inversions for sea ice thickness and conductivity from electromagnetic induction data: Inclusion of nonlinearities caused by passive bucking

Priska A. Hunkeler[1], Stefan Hendricks[1], Mario Hoppmann[1], Colin G. Farquharson[2], Thomas Kalscheuer[3], Melchior Grab[4], Manuela S. Kaufmann[4], Lasse Rabenstein[4], and Rüdiger Gerdes[5]

ABSTRACT

The porosity of sea ice is a fundamental physical parameter that governs the mechanical strength of sea ice and the mobility of gases and nutrients for biological processes and biogeochemical cycles in the sea ice layer. However, little is known about the spatial distribution of the sea ice porosity and its variability between different sea ice types; an efficient and nondestructive method to measure this property is currently missing. Sea ice porosity is linked to the bulk electrical conductivity of sea ice, a parameter routinely used to discriminate between sea ice and seawater by electromagnetic (EM) induction sensors. Here, we have evaluated the prospect of porosity retrieval of sea ice by means of bulk conductivity estimates using 1D multifrequency EM inversion schemes. We have focused on two inversion algorithms, a smoothness-constrained inversion and a Marquardt-Levenberg inversion, which we modified for the nonlinear signal bias caused by a passive bucking coil operated in such a highly conductive environment. Using synthetic modeling studies, 1D inversion algorithms and multiple frequencies, we found that we can resolve the sea ice conductivity within ± 0.01 S/m. Using standard assumptions for the conductivity-porosity relation of sea ice, we were able to estimate porosity with an uncertainty of $\pm 1.2\%$, which enables efficient and nondestructive surveys of the internal state of the sea ice cover.

INTRODUCTION

Along with the shrinking sea ice extent (Stroeve et al., 2012; Comiso and Hall, 2014), Arctic sea ice is thinning (Lindsay and Zhang, 2005; Haas et al., 2008; Kwok et al., 2009) and becoming younger (Maslanik et al., 2011). The change toward a younger sea ice cover leads to changes in the average internal structure. For example, first-year sea ice shows higher absorption rates of shortwave radiation than does older sea ice, leading to a stronger internal warming and melting (Perovich et al., 2011; Nicolaus et al., 2012). This in turn results in an increase of the connectivity of pores and brine channels, which governs the exchange of gases (Gosink et al., 1976) and nutrients (Krembs et al., 2011) and the mechanical strength (Kovacs, 1996). Here, we develop and present a methodology to improve the use of electromagnetic (EM) induction sounding instruments to retrieve information related to the internal structure of different sea ice types, based on the measurements of bulk electrical sea ice conductivity, hereinafter referred to as conductivity.

The conductivity and porosity of a sea ice layer are generally linked (Archie, 1942). Pores of young sea ice are usually filled with highly saline brine left from the formation process, whereas in older, multiyear sea ice, this brine is usually replaced by freshwater due to meltwater flushing (Eicken et al., 2002; Vancoppenolle et al., 2007) or gravity drainage (Niedrauer and Martin, 1979; Notz and Worster, 2008). This also means that older, multiyear sea ice is electrically more resistive, whereas young, porous sea ice still has a high conductivity due to brine inclusions. Summer sea ice often shows macroscale pores because brine channels are widened and connected by melt processes. These pores then contain a mix of meltwater and brine, which change the geochemistry of sea ice and the availability of nutrients for biological processes (Thomas and Dieckmann, 2009; Vancoppenolle et al., 2010). Mapping sea ice layer porosity by proxy measurements of sea ice conductivity would therefore enable improved process studies of sea ice mass balance and especially complex biogeochemical cycles through the atmosphere/sea ice/ocean interfaces. Information on the spatial variability, large-scale gradients, and the annual cycle of internal sea ice properties is only sparsely available (e.g., Golden et al., 2007; Pringle et al., 2009). Current methods to obtain information on sea ice porosity are based on manual coring, whereas the high spatial variability in the sea ice cover calls for a rapid and nondestructive method.

The conductivity of sea ice, and in particular its large contrast with that of the ocean, is routinely used for sea ice thickness retrieval by frequency-domain EM induction sounders, which usually use a single frequency in a range from 4 to 10 kHz. This method is deployed from helicopters (Kovacs and Holladay, 1990; Haas et al., 2009), aircraft (Haas et al., 2010), ship-mounted booms (Haas, 1998; Reid et al., 2003), or directly on the sea ice surface for high-resolution case studies (Eicken et al., 2001; Haas, 2004; Druckenmiller et al., 2009; Weissling et al., 2011). The retrieval algorithm assumes that sea ice and snow can be described as a single, flat 1D layer, which is usually the case for level sea ice, and that the effect of sea ice and snow conductivity on the EM response is negligible compared with the contribution from the underlying seawater. The EM response can be approximated with an exponential relation to the distance of the sea ice/seawater interface of either the in-phase or quadrature (out-of-phase) component, parameterized from calibration measurements or 1D forward models. The inverse of the exponential function then directly relates the EM response to the total thickness (snow and sea ice) for the given height of the sensor above the surface (Kovacs and Morey, 1991). We refer to this method as *empirical exponential* (EMPEX) according to Pfaffling et al. (2007). This approach has proven to be a robust methodology for empirical sea ice thickness retrieval, but it inherently has to neglect any changes of the sea ice conductivity.

The assumption of a perfectly resistive, single layer of sea ice and snow is justified in most cases because the influence of the sea ice conductivity of dry, cold, level sea ice with typical thicknesses of 1–2 m is small in the traditionally used frequency range (Pfaffling and Reid, 2009). However, there are cases in which the sea ice conductivity is desired for sea ice type classification and even becomes a dominant factor, e.g., for summer melt conditions or the so-called subice platelet layer. The latter is a layer of loose ice crystals (ice platelets) with a bulk conductivity between those of sea ice and ocean water (Rack et al., 2013; Hunkeler et al., 2015), and it may be located underneath coastal sea ice in Antarctica. Ice platelets originate from supercooled water in cavities below ice shelves and

are a main contributor to the local sea ice mass balance. A mapping of this special sea ice type is still a challenge due to the scarcity of available data (Hoppmann et al., 2015; Langhorne et al., 2015). In addition, the sea ice thickness can vary on instrument subfootprint scales, and not all sea ice structures can be sufficiently described by a 1D geometry approximation within the footprint. The traditional 1D assumption leads to thickness biases for deformed sea ice, partly due to the geometric effect of subfootprint-scale thickness variability (Kovacs et al., 1995; Reid et al., 2003; Pfaffhuber et al., 2012) and partly due to the intrusion of saline seawater into the sea ice layer (Reid et al., 2006).

Operational needs for in situ high-resolution sea ice surveys require a small sensor package that can be towed by a person on foot or by snowmobile. It is a particular characteristic of such surveys that measurements are taken in a highly conductive environment given that the sensor is usually a few meters above seawater. The conductivities of sea ice layers we aim to resolve ($0.01 - 0.2$ S/m) can be 1–2 orders of magnitude smaller than the conductivity of the ocean (e.g., 2.7 S/m). Distances between the sensor and the saline ocean water can easily become smaller than the dimensions of the sensor itself. Previous EM sea ice studies have accounted for sea ice conductivities, such as Pfaffling and Reid (2009), who reveal that the lower frequency (3.68 kHz) of an airborne device is mostly sensitive to sea ice thickness, whereas higher frequencies (112 kHz) are needed to resolve sea ice conductivity. However, the difference in conductivity between first-year sea ice (0.05 S/m) and multiyear sea ice (<0.01 S/m) could not be resolved for sea ice thinner than 2 m. In contrast, Holladay et al. (1998) use airborne EM induction sounding to distinguish between first- and multiyear sea ice using 30 and 90 kHz. Reid et al. (2003) conclude that it is necessary for sea ice thickness retrieval to account for conductive sea ice.

Empirical analytic approaches for processing single-frequency EM data are insufficient to resolve thickness and conductivity of even a single layer. Therefore, we assess the prospect of using 1D inversion algorithms on multifrequency EM data, in which (1) conductivity within fixed layers and (2) conductivity and thickness of sea ice layers are adapted to minimize the difference between the signal response and forward models. Previously, Hunkeler et al. (2015) perform case studies with a ground-based device (GEM-2, Geophex Ltd.) at frequencies of 63.03 and 93.09 kHz and a coil spacing of 1.66 m, being able to resolve sea ice conductivities in agreement with estimates from sea ice cores. The assessment of sea ice conductivity in this study is based on the same small-coil instrument in which *small coil* refers to the transmitter (Tx) and receiver (Rx) coils that have small diameters compared with the distance between them. Hence, the magnetic field generated by the transmitter is represented by a magnetic dipole, and the measurements at the Rx are considered to be point measurements of the magnetic field (Farquharson, 2000). Processing routines of data from such small-coil instruments in highly conductive environments cannot be based on existing algorithms because of a nonlinear signal bias introduced by the passive bucking coil (Bx) of the instrument. This coil is used to null the primary field at the receiver location and effectively acts as a second receiver. In low-conductivity environments, the contribution of this second receiver can safely be approximated by a linear factor and the correction is often integrated in the sensor calibration. However, the contribution of the Bx significantly depends on the subsurface conductivity itself (Fitterman, 1998) and needs to be taken into account

in the forward model and inversion scheme in highly conductive regimes.

In this study, we applied two modified geophysical inversion algorithms that specifically include the Bx. We used synthetic data and specific instrumental noise characteristics to run inversions for different thickness and conductivity scenarios as a proof of concept for the application to actual field data. We analyzed the sensitivity of the inversion results and their success in resolving sea ice thickness and conductivity simultaneously. Finally, the porosity and its uncertainty is estimated from conductivity retrievals.

METHODS

We first describe principles behind multifrequency measurements and passive EM bucking, then review two inversion algorithms with the implemented Bx correction for a small-coil EM instrument.

Multifrequency measurements with small-coil systems

The quasi-static near-field zone (Spies and Frischknecht, 1991) is defined by the transmitter-receiver distance x_{Rx} being much smaller than the quasi-static plane-wave skin depth δ, which is defined as follows:

$$\delta = \sqrt{\frac{2}{\omega\mu\sigma}}, \tag{1}$$

where ω is the angular frequency ($\omega = 2\pi f$), μ is the magnetic permeability of free space ($\mu = 4\pi 10^{-7}$ H/m), and σ is the conductivity. In the near-field zone using the same transmitter-receiver geometry, measurements at multiple frequencies do not add information over a single-frequency measurement unless the conductivity shows a frequency dependence. To increase the sounding depth, the transmitter-receiver distance has to be increased or the coil orientation has to be changed. The quasi-static transition zone corresponds to measurements with $x_{Rx} \sim \delta$. Compared with measurements in the near-field zone, the sounding depth increases additionally with decreasing frequency (Spies and Frischknecht, 1991). This results in additional information being retrieved using different frequencies.

The lower frequencies considered in our study, i.e., $f_1 = 1.53$ and $f_2 = 5.31$ kHz, represent measurements in the near-field zone. For instance, for measurements at frequency f_1, the skin depths in seawater (conductivity of 2.7 S/m) and sea ice of 0.2 S/m are $\delta = 7.8$ and $\delta = 28.8$ m, respectively. Both skin depths are significantly larger than the transmitter-receiver separation of 1.66 m. However, measurements at higher frequencies; i.e., $f_3 = 18.33$, $f_4 = 63.03$, and $f_5 = 93.09$ kHz are effectively in the transition zone. For frequency f_5, $\delta = 1.0$ and $\delta = 3.6$ m for seawater and sea ice with a conductivity of 0.2 S/m, respectively. This suggests that in highly conductive sea ice environments, EM soundings by varying frequency are feasible even at transmitter-receiver separations as small as 1.66 m. Moreover, in our case of a moderately conductive layer being underlain by a highly conductive layer, resolution of layer parameters is generally much better than in the opposite case of a highly conductive layer being underlain by a moderately conductive layer (Spies and Frischknecht, 1991).

Passive EM bucking

Current EM induction instruments operate at single to multiple discrete frequencies. A typical EM instrument consists of three coils (Figure 1): Tx, Bx, and Rx. The Tx generates a primary magnetic field inducing a secondary magnetic field in a conductive subsurface. The signal strength of this secondary field depends, among other things, on the distance from the instrument to a body and its conductivity. During a survey, the Rx records the superposition of the primary and secondary magnetic fields minus the bucking field.

The purpose of a Bx is to null the primary field at the receiver, which also avoids receiver saturation, and increases the dynamic range of the instrument (Won et al., 2003). It is connected in series and in opposite polarity to the Rx and technically acts as a second receiver. In free space, the Bx measures the same absolute primary field signal as does the Rx when the following relation according to Won et al. (2003) is valid:

$$\frac{A_{Rx}n_{Rx}}{x_{Rx}^3} = \frac{A_{Bx}n_{Bx}}{x_{Bx}^3}, \tag{2}$$

where x_{Bx} is the distance between Tx and Bx, x_{Rx} is the distance between Tx and Rx, and A and n are the area and number of turns of the respective coil. Typically, x_{Bx} and x_{Rx} are on the order of 1–4 m, e.g., one particular commercial realization has $x_{Bx} = 1.035$ m and $x_{Rx} = 1.66$ m and accommodates simultaneous operation at 0.3–96 kHz. The Bx, which is assumed to be linearly sensitive to the conductive subsurface, compensates internally for the primary field at the receiver location. However, in the seawater environment, the response of the Bx to the secondary field is nonlinear, leading to an overcorrection of the receiver signal depending on the conductivity structure of the subsurface (Fitterman, 1998). Hunkeler et al. (2015) account for this so-called bucking bias by modifying the forward modeled data according to

$$\mathbf{d} = \mathbf{d}_{Rx} - \mathbf{d}_{Bx} = (\mathbf{I}_{Rx} + i\mathbf{Q}_{Rx}) - (\mathbf{I}_{Bx} + i\mathbf{Q}_{Bx}), \tag{3}$$

Figure 1. Diagrammatic sketch of multifrequency EM device on level sea ice. (a) Two exemplary stations with different sea ice thicknesses. Synthetic data were calculated by assuming level sea ice thicknesses t_{syn} from 0 to 10 m in increments of 0.1 m and conductivities σ_{syn} of 0.01, 0.05, 0.10, 0.15, and 0.20 S/m. (b) Internal coil configuration and frequencies used for calculation of synthetic data, x_{Rx} and x_{Bx} are the distances from the Tx to the Rx and Bx, respectively. The Bx is used to null the primary field at the receiver location. Algorithms needed to be modified for a nonlinear bucking bias arising from measurements in highly conductive regimes.

where $\mathbf{d}$ is the signal response at the Rx ($\mathbf{d}_{Rx}$) and Bx ($\mathbf{d}_{Bx}$) locations. These signals can also be expressed as a complex number with real (in-phase I) and imaginary parts (quadrature Q), in which I and Q are dimensionless and measured in parts per million (ppm). An alternative representation of the signal is by its amplitude $A = \sqrt{I^2 + Q^2}$ and phase $\varphi = \arctan(Q/I)$. Hunkeler et al. (2015) achieve a satisfying agreement between field data and corrected forward modeled data by applying coefficients obtained from calibration experiments. In this study, we build on these findings to implement the Bx into two different inversion algorithms.

Inverse modeling

The aim of an inversion algorithm is to find a plausible model of the subsurface (usually the simplest), which adequately fits the observed data within the data uncertainty (Farquharson et al., 2003). The process consists of two components: forward modeling and inversion. Forward modeling generates the data of a specific model, whereas inversion automatically changes the model to reduce the misfit between the measured and forward-modeled data (Menke, 1989). We tested two inversion algorithms to resolve synthetic data of homogeneous sea ice for different thicknesses and conductivities. Forward modeling and inversion calculations were performed in 1D. We stitched the 1D inversion results of individual stations, which results in a 2D impression. With the first algorithm (EM1DFM, Farquharson [2000] and Farquharson et al. [2003]), we only inverted for the conductivity within fixed layers of 0.1-m thickness using vertical smoothing between layers. Hence, we call this inversion algorithm smoothness-constrained inversion. Because a vertical conductivity smoothing is not ideal in the case of a sharp sea ice/seawater interface, we applied a second algorithm, the Marquardt-Levenberg inversion (Jupp and Vozoff, 1975; Lines and Treitel, 1984). With only two distinct (instead of many individual) layers and with sea ice thickness as an additional free parameter, this scheme may better reflect reality. In our study, we used the Marquardt-Levenberg inversion algorithm from EM inversion with least intricate algorithms (EMILIA, Kalscheuer et al. [2010, 2012] and Grab [2012]).

Smoothness-constrained inversion (EM1DFM)

The inversion problem is ill posed and nonlinear. Therefore, we derived at each iteration n a linearized approximation by searching for a change in the conductivity model that minimizes the cost function

$$\Phi^n = \phi_d^n + \beta^n \phi_m^n, \tag{4}$$

where ϕ_d is the data misfit, β is the trade-off parameter, and ϕ_m is the model-structure component (Farquharson et al., 2003). The data misfit ϕ_d is calculated according to Farquharson et al. (2003) by the l_2 norm

$$\phi_d^n = \|\mathbf{W}_d(\mathbf{d}^n - \mathbf{d}_{syn})\|^2, \tag{5}$$

where $\mathbf{d}_{syn}$ is the synthetic EM data. The quantities $\mathbf{d}^n$ are the forward-modeled data for the model $\mathbf{m}^n$ of the nth iteration, where $\mathbf{d}^n$ is defined as the nonlinear forward operator $\mathbf{F}[\mathbf{m}^n]$. By accounting for the bucking bias, $\mathbf{d}_{syn}$ and $\mathbf{d}^n$ need to be modified according to equation 3. The quantity $\mathbf{W}_d$ is a diagonal weighting matrix. For the

Bx quantification (experiment 1; see below), $\mathbf{W}_d$ includes the reciprocal value of 1% of the synthetic data. For the synthetic modeling studies (experiments 2–4; see below), $\mathbf{W}_d$ includes the reciprocal standard deviations of the data, which were calculated from 30 min of free-air recordings of noise at each frequency for in-phase and quadrature components (Hunkeler et al., 2015).

The model-structure component in equation 4 is defined by

$$\phi_m^n = \alpha_s \|\mathbf{W}_s \mathbf{m}^n\|^2 + \alpha_z \|\mathbf{W}_z \mathbf{m}^n\|^2, \tag{6}$$

where $\mathbf{m}$ is the model vector of the logarithms of the layer conductivities and α_s ($= 0.05$) and α_z ($= 1$) are scaling coefficients. The diagonal matrix $\mathbf{W}_s$ contains elements that are equal to the square roots of the individual layer thicknesses ($= 0.1$ m). The matrix $\mathbf{W}_z$ is a first-order finite-difference operator. The rows are scaled by the reciprocals of the square roots of half the distance between the centers of two layers (Farquharson et al., 2003). The left term in equation 6 quantifies the deviation from a reference model of 1 S/m, whereas the right term indicates the roughness of the model. Since α_s is significantly smaller than α_z, the right term dominates the model-structure component.

The trade-off parameter β (equation 4) determines the balance between the data misfit and the model-structure component and is responsible for fitting the observed data closely, whereas the constructed model should be as simple as possible (Farquharson et al., 2003). The noise is well known. Therefore, we adjusted β with a univariate search until the misfit ϕ_d matched a predefined target misfit in every iteration n. This is the maximum of the number of the calculated responses $N_d = 10$ (in-phase and quadrature for the five frequencies), or equal to $0.5\phi_d^{n-1}$, to allow only small changes in model structure at each iteration (discrepancy principle, Farquharson, 2000). In case the target misfit cannot be reached, the inversion algorithm searches for the smallest misfit.

The new model $\mathbf{m}^n$ is calculated from the previous model $\mathbf{m}^{n-1}$ by

$$\mathbf{m}^n = \mathbf{m}^{n-1} + \upsilon \delta \mathbf{m}^n, \tag{7}$$

where $\delta \mathbf{m}$ is the model update step and υ is the step length, which is halved when the cost function (equation 4) does not immediately decrease. To find the model update step $\delta \mathbf{m}$, equation 4 is differentiated with respect to $\delta \mathbf{m}$, set equal to zero, and solved by a least-squares approach for $\delta \mathbf{m}$ (Paige and Saunders, 1982; Farquharson et al., 2003). By doing so, the forward-modeled data $\mathbf{d}^n$ in equation 5 are approximated in the derivation of the inversion algorithm by

$$\mathbf{d}^n \approx \mathbf{d}^{n-1} + \mathbf{J}^{n-1} \delta \mathbf{m}^n, \tag{8}$$

where $\mathbf{J}$ is the Jacobian matrix of sensitivities (Farquharson and Oldenburg, 1996). The $\mathbf{J}$ consists of the partial derivatives of the data with respect to the model parameters (logarithms of conductivities σ) for the jth layer and ith station:

$$J_{ij}^n = \frac{\partial d_{Rx,i}}{\partial \log \sigma_j^n} - \frac{\partial d_{Bx,i}}{\partial \log \sigma_j^n}, \tag{9}$$

where d is the signal response at the Rx (d_{Rx}) and Bx (d_{Bx}) locations. These sensitivities quantify how the forward-modeled data are affected by changing the conductivity of each layer (Farquhar-

son and Oldenburg, 1993). The second term in equation 9 is not required if the Bx modification is to be ignored.

To evaluate the compatibility of the new model $\mathbf{m}^n$ with the field data, the full forward response $\mathbf{d}^n = \mathbf{F}[\mathbf{m}^n]$ is then used to calculate ϕ_d (not the approximation in equation 8). The convergence of the inversion algorithm is determined using two convergence criteria according to Gill et al. (1981) and Farquharson (2000).

To assess how well synthetic data for a constructed model fit the measured data, we calculated the root-mean square (rms) error, such that

$$\text{rms error} = \sqrt{\frac{1}{N_d}\phi_d}. \qquad (10)$$

An inversion with rms error close to one is considered reliable without fitting too much to noise (Kalscheuer et al., 2013).

Marquardt-Levenberg inversion (EMILIA)

The Marquardt-Levenberg algorithm of EMILIA was recently modified to account for the Bx bias by the implementation of equations 3 and 9 (Kaufmann, 2014). The cost function Φ is similar to equation 4. The quantity ϕ_d is defined in a similar manner to equation 5 (more below). The quantity β governs the magnitude of the damping and specifies the confidence in the previous model (damping factor). The quantity ϕ_m is now defined as

$$\phi_m^n = \|(\mathbf{m}^n - \mathbf{m}^{n-1})\|^2 \qquad (11)$$

for the nth iteration. Since differences between the new model $\mathbf{m}^n$ and the previous model $\mathbf{m}^{n-1}$ are penalized, the inversion result is influenced by the starting model. The starting model is the first assumed subsurface model with the defined thicknesses and conductivities of sea ice and underlying seawater, which is adapted during the inversion process. To improve sea ice thickness results from the Marquardt-Levenberg inversion, we weighted the data misfit ϕ_{dw} according to Kalscheuer et al. (2013):

$$\phi_{dw}^n = \sum_{i=1}^{N_s} \left\| \frac{\mathbf{W}_{d,i}(\mathbf{d}_i^n - \mathbf{d}_{\text{syn},i})}{w_i^2} \right\|^2, \qquad (12)$$

where N_s is the number of stations, and the weight factors w_i are obtained from normalized synthetic data of one frequency and one component and are kept constant over the course of the iterations. Small values of w_i were assigned to stations of thick sea ice to increase their weights. The misfit ϕ_{dw} is normalized by the sum of the squared weight factors w^2 to achieve the intended total weighted rms error (rms error$_w$) of 1, where

$$\text{rms error}_w = \sqrt{\frac{1}{\sum_{i=1}^{N_s} \frac{N_{d,i}}{w_i^2}}\phi_{dw}}, \qquad (13)$$

and $N_{d,i}$ is the number of calculated responses of station i. For rms error > 1, a line search is performed for β and the model is adapted accordingly. To assess the data fit of a particular station, the sums in equations 12 and 13 are limited to that station.

Most-squares inversion

We applied a model error and resolution analysis to some of our two-layer Marquardt-Levenberg inversions. This method is based on the truncated singular value decomposition (TSVD) of the sensitivity matrix (Kalscheuer and Pedersen, 2007). Because the effective number of model parameters is two (conductivity σ and thickness t of sea ice), the truncation level of the TSVD is set to two in the analyses of these models. Due to the very limited number of model parameters, both layer parameters are perfectly resolved. Hence, in assessing how well the layer parameters are constrained, only the model parameter uncertainties need to be further considered.

To partly account for the nonlinearity of the inversion problem, we computed error estimates for the final inversion models using most-squares inversion (Jackson, 1976; Meju and Hutton, 1992; Meju, 1994). A most-squares inversion is an iterative method that, starting from the least-squares inversion results, determines bounding model values that represent the variability of the model parameters. The goal is to assess the stability of model parameters (Meju and Hutton, 1992). Owing to the logarithmic transformation of model parameters during inversion, the most-squares errors, $1/f_{\text{MSQ}}^-$ and f_{MSQ}^+, correspond to parameter ranges $\sigma/f_{\text{MSQ}}^-, \ldots, f_{\text{MSQ}}^+ \cdot \sigma$ and $t/f_{\text{MSQ}}^-, \ldots, f_{\text{MSQ}}^+ \cdot t$ of layer conductivities and thicknesses, respectively. Hence, a model parameter is well constrained with most-squares errors close to one.

Synthetic data

To test the inversion algorithms, we used synthetic data sets for the in-phase and quadrature components, calculated by a 1D forward model using the implementation of Anderson (1979). We calculated two different types of synthetic data sets: (1) neglecting ($\mathbf{d}_{\text{syn}} = \mathbf{d}_{\text{Rx}}$) and (2) accounting ($\mathbf{d}_{\text{syn}} = \mathbf{d}_{\text{Rx}} - \mathbf{d}_{\text{Bx}}$) for the Bx correction according to equation 3. One data set includes 101 stations, in which the sea ice was increased from 0 to 10 m from one station to the next in increments of 0.1 m. These true thicknesses are hereinafter referred to as t_{syn}. Two exemplary stations are illustrated in Figure 1a, in which a snow layer was neglected. We used typical conductivities σ_{syn} of different sea ice types between 0.01 and 0.2 S/m (Hunkeler et al., 2015) and a homogeneous half-space conductivity of 2.7 S/m, representing seawater. In-phase and quadrature responses were calculated at frequencies of 1.53, 5.31, 18.33, 63.03, and 93.09 kHz, a setup also used during surveys on sea ice (Hunkeler et al., 2015). For this proof-of-concept of the Bx implementation, we did not account for any noise of the instrument (experiment 1). To simulate realistic data, we added Gaussian noise (corresponding to one standard deviation) to the in-phase and quadrature components based on the free-air response for the respective frequencies (experiments 2–4). The assumed standard deviations between 125 and 204 ppm were calculated by Hunkeler et al. (2015), in which higher frequencies showed higher instrumental noise. The synthetic data from the implementation of Anderson (1979) were compared with the data forward modeled by the inversion algorithms considered here. The data sets computed by all three programs differed only by a few ppm, which is well within the noise level of the instrument.

RESULTS

We applied the two inversion algorithms to synthetic data calculated for stations with variable sea ice thickness and conductivity.
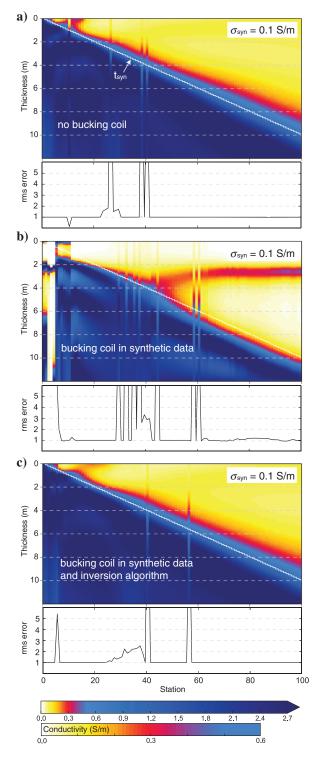
Figure 2. Influence of the bucking bias on sea ice thickness and conductivity retrieval (experiment 1). Each station represents a smoothness-constrained 1D inversion result (EM1DFM). The Bx modification was applied to (a) neither synthetic data nor inversion (scenario s1), (b) only synthetic data (scenario s2), and (c) synthetic data and inversion (scenario s3). The colored regions show the resulting conductivities, from which we infer the sea ice thickness. The σ_{syn} of 0.1 S/m, seawater conductivity of 2.7 S/m and t_{syn} (white steps) were reproduced best for scenarios s1 and s3. Below each scenario, the rms error is shown for all stations. The target misfit was reached when the rms error = 1.

We first identify the impact of the Bx on the performance of the EM1DFM inversion (experiment 1). We then investigate whether multilayered, Marquardt-Levenberg inversions are able to reliably reproduce t_{syn} and σ_{syn} (experiments 2–4).

Experiment 1: Influence of bucking coil

We used two synthetic data sets, with and without bucking bias, and two versions of EM1DFM, ignoring and considering the bucking bias. We tested the following three scenarios: (1) bucking bias neither in the data nor considered in EM1DFM, (2) bucking bias in the data but not considered in EM1DFM, and (3) bucking bias in the data and considered in EM1DFM. For all calculations, we used $\sigma_{syn} = 0.1$ S/m, a seawater conductivity of 2.7 S/m, and t_{syn} of 0–10 m. For the starting model, we assigned to all stations 1-m-thick sea ice with conductivities of 0.05 and 2.7 S/m to the underlying seawater. We allowed a maximum of 40 iterations and set the uncertainties in $\mathbf{W}_d$ to 1% of the synthetic data.

For the first scenario, the rms error (equation 10) was close to one for most inversions, whereas a rms error > 2 was found for only three stations (Figure 2a). Although the level of agreement between inversion results and the synthetic data was generally good, an accurate determination of sea ice thickness from these stations was difficult because conductivities varied little between vertically adjacent layers, resulting in a smooth conductivity transition between sea ice and seawater. This transition zone from sea ice to seawater conductivities was small for thinner sea ice ($t_{syn} < 4$ m, white steps in Figure 2a), but widened toward thicker sea ice (3 m for $t_{syn} = 10$ m). Apart from this variable transition zone, σ_{syn} of 0.1 S/m (yellow in Figure 2a) and seawater conductivity of 2.7 S/m (blue in Figure 2a) were reasonably reproduced.

We used for the second scenario the same setup as for the first scenario, and we included the bucking bias in the synthetic data (equation 3; Figure 2b), but not in the inversion algorithm. The algorithm completely failed to reproduce the data for $t_{syn} < 0.5$ m, in which high rms errors indicated that the target misfit was often not achieved. For t_{syn} between 0.5 and 1 m, the algorithm added an additional conductive layer close to the surface. Between 0.5 and 10 m, the transition zone was approximately 1 m too deep compared with t_{syn}. The $\sigma_{syn} = 0.1$ S/m was only rarely reproduced with sea ice conductivity in individual fixed layers being either too high (approximately 0.3 S/m, red in Figure 2b) or too low (close to 0 S/m, white in Figure 2b). For $t_{syn} > 5$ m, the algorithm added a conductive layer in the middle of the too-resistive sea ice.

For the third scenario, we used the modified synthetic data from the second scenario together with the modified EM1DFM inversion algorithm (equations 3 and 9). The results (Figure 2c) showed a substantial improvement over the second scenario (Figure 2b), in which the rms error and the resolved sea ice thickness and conductivity were comparable with those from the first scenario. For $t_{syn} < 0.5$ m, conductivities similar to the underlying seawater indicate that σ_{syn} could not be resolved.

For all further experiments, we included the Bx in the synthetic data and inversions.
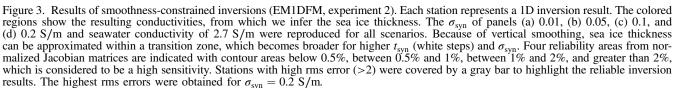
Experiment 2: Smoothness-constrained inversion

In a second experiment, we used synthetic data with added Gaussian noise and $\sigma_{syn} = 0.01, 0.05, 0.1,$ and 0.2 S/m. For each σ_{syn},
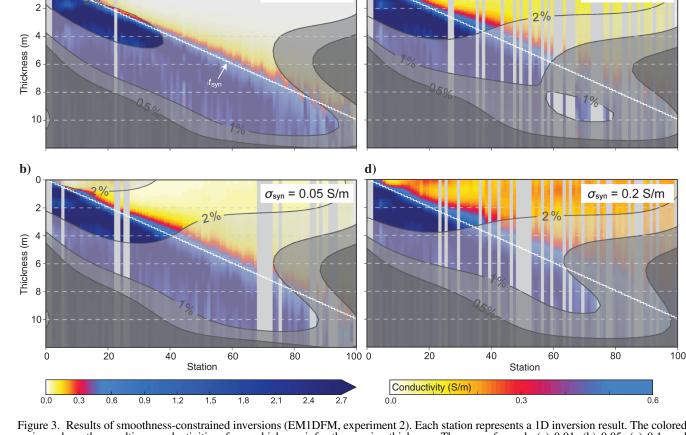
we calculated the EM response for thicknesses t_{syn} of 0–10 m. The starting model for each station contained 3 m of 0.05 S/m (sea ice) and an underlying homogeneous half-space of 2.7 S/m (seawater). The uncertainty was set to one standard deviation of the noise, and a maximum of 40 iterations was allowed. At all stations, the algorithm stopped before 40 iterations, either because convergence to the target misfit or a minimum was reached, or no suitable model update step was found.

The results of the four scenarios generally showed a good agreement with the synthetic data (Figure 3). The number of stations for which the target misfit could not be achieved were 3, 19, 31, and 29 for σ_{syn} of 0.01, 0.05, 0.1, and 0.2 S/m, respectively. For all inversions, the first two stations with t_{syn} of 0 and 0.1 m showed high rms errors (> 2). However, for stations with rms error < 2, sea ice thickness was reasonably resolved for all four scenarios, but the transition zone between sea ice and seawater conductivity became broader for higher σ_{syn}. At station 30 with 3-m-thick sea ice, for example, the zone was for $\sigma_{syn} = 0.01$ S/m only 0.5 m (Figure 3a), whereas for $\sigma_{syn} = 0.2$ S/m, it was 1 m wide (Figure 3d). The resulting sea ice conductivity was also more uni-

form for low σ_{syn} (Figure 3a) compared with the patchy conductivity results from higher σ_{syn} (Figure 3d). However, the sea ice conductivities were clearly distinguishable for the individual scenarios and can be resolved well within 0.05 S/m using EM1DFM.

For each of the four scenarios, we obtained after the last iteration 10 Jacobian matrices of sensitivities (equation 9) from the five frequencies and both components (in-phase and quadrature). Each Jacobian matrix includes entries at every station in each layer for the respective scenario. To provide a quantified reliability estimate, we normalized all entries of the Jacobian matrices by the respective forward modeled data $\mathbf{d}$ obtained after the last iteration. From the calculated normalized Jacobian matrices, we selected for each layer the maximum of the 10 entries. Here, we show for each scenario the resulting 0.5%, 1%, and 2% contour lines, along with the four resulting reliability areas (shaded areas in Figure 3). Small values of normalized Jacobian matrices indicate that a change in the conductivity barely affects the forward modeled data (Farquharson and Oldenburg, 1993); hence, we trust regions with high sensitivities most.

Figure 3. Results of smoothness-constrained inversions (EM1DFM, experiment 2). Each station represents a 1D inversion result. The colored regions show the resulting conductivities, from which we infer the sea ice thickness. The σ_{syn} of panels (a) 0.01, (b) 0.05, (c) 0.1, and (d) 0.2 S/m and seawater conductivity of 2.7 S/m were reproduced for all scenarios. Because of vertical smoothing, sea ice thickness can be approximated within a transition zone, which becomes broader for higher t_{syn} (white steps) and σ_{syn}. Four reliability areas from normalized Jacobian matrices are indicated with contour areas below 0.5%, between 0.5% and 1%, between 1% and 2%, and greater than 2%, which is considered to be a high sensitivity. Stations with high rms error (>2) were covered by a gray bar to highlight the reliable inversion results. The highest rms errors were obtained for $\sigma_{syn} = 0.2$ S/m.

Experiment 3: Marquardt-Levenberg inversion and most-squares inversion

We inverted the same synthetic data used in the second experiment (including Gaussian noise) by the Marquardt-Levenberg algorithm. The data uncertainty was again set to the standard deviation of the noise, and we used a starting model for each station of 0.05 S/m for the upper 3 m (sea ice) and 2.7 S/m for the homogeneous half-space below (seawater). The latter was fixed during this inversion because seawater conductivity is usually known and can be determined with tight bounds by sampling through bore-

holes. In the eastern Weddell Sea, for example, the seawater conductivity ranged from 2.686 to 2.718 S/m over a time period of roughly three months (Hunkeler et al., 2015) and is usually assumed to be constant during a survey. Tests showed that the Marquardt-Levenberg inversion performed considerably worse when allowing for a free seawater conductivity. Therefore, only sea ice thickness t and sea ice conductivity σ were allowed to vary during a maximum of 300 iterations.

After the maximum of iterations was reached, t was for $t_{syn} < 5$ m well resolved for all four scenarios (Figure 4). The
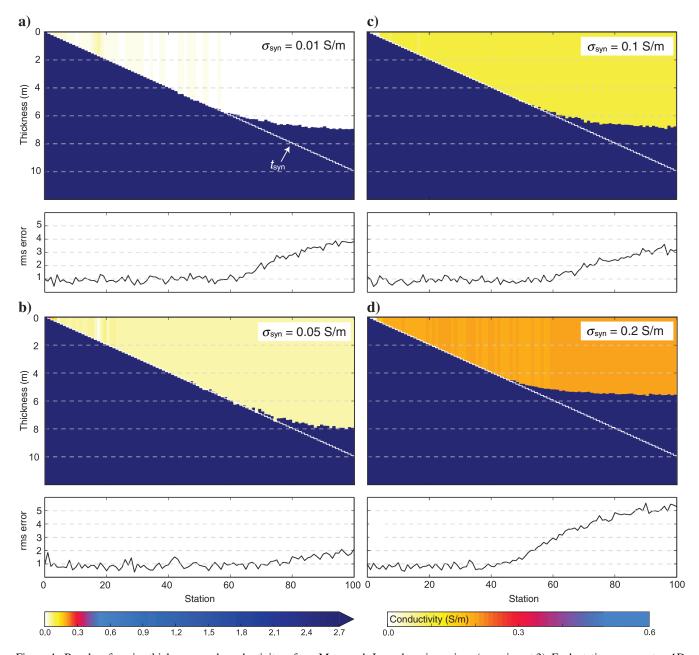

Figure 4. Results of sea ice thickness t and conductivity σ from Marquardt-Levenberg inversions (experiment 3). Each station represents a 1D inversion result. The colored regions show the resulting conductivities σ, from which we directly obtain the sea ice thickness t. The σ_{syn} of panels (a) 0.01, (b) 0.05, (c) 0.1, and (d) 0.2 S/m was reproduced for all four scenarios. The t_{syn} (white steps) was better reproduced for panels (a-c) compared with panel (d). Below each scenario, the rms error is shown for individual stations, in which the rms error increases in all scenarios with higher t_{syn}, which causes smaller signal responses.

rms error was generally higher for thicker sea ice compared with thinner sea ice in all scenarios. Most stations with a high rms error were found for $\sigma_{syn} = 0.2$ S/m, whereas the inversion of approximately half of the stations yielded a rms error > 1 (Figure 4d). The lowest rms error and accurately reproduced t (for $t_{syn} < 7$ m) were found for the inversions with $\sigma_{syn} = 0.05$ S/m, which is also the conductivity defined in the starting model (Figure 4b).

To quantify these findings, we compared the inversion results (and results with $\sigma_{syn} = 0.15$ S/m) to t_{syn} (Figure 5a, scenarios s1–s5). The best resolved sea ice thickness t was found, as stated before, for $\sigma_{syn} = 0.05$ S/m (s2). However, t was generally reasonably reproduced for $t_{syn} < 5$ m in all scenarios.

For comparison to resulting sea ice thickness t, we calculated thicknesses with the EMPEX approach. For the latter, we used the 5310 Hz in-phase forward responses, added Gaussian noise, and fitted a single-exponential curve through the data (in-phase response versus sea ice thickness). This curve fit represents the exponential function that is normally calculated from calibration measurements in the field. We used the in-phase component because it is more sensitive to deeper structures, and it is, in contrast to the quadrature component, monotonically decreasing with thickness. The noise of the data was larger than the changes of the exponential function for thick sea ice with low signal responses. Hence, large sea ice thicknesses were poorly constrained. Because the exponential function was not approaching zero, a corresponding sea ice thickness could not always be found for low signal responses and sea ice > 8 m (Figure 5b).

In general, sea ice thickness t was underestimated with the Marquardt-Levenberg inversion, but overestimated with the calculated exponential function. With both methods, reliable results were found for sea ice < 5 m. For thicker sea ice, the Marquardt-Levenberg inversion depended on σ_{syn}, on the starting model and the weighting of the data (more below). The sea ice thickness determination by the exponential approach did not depend on sea ice conductivity because we calculated the exponential fit from the respective in-phase components.

The sea ice conductivity σ, however, could be resolved for scenarios s1–s5 (Figure 5a). Figure 5c shows distributions of σ, in which individual histograms are clearly separated. For the scenario with the best resolved sea ice thickness t (s2), the narrowest conductivity distribution was found (0.05 S/m in Figure 5c). For scenarios s1–s5, the interquartile ranges of σ were within 0.01 S/m (Figure 5d).

In Table 1, we present the estimated model errors from most-squares inversion of the Marquardt-Levenberg inversion models for stations 11 and 31 (t_{syn} of 1 and 3 m) for $\sigma_{syn} = 0.05$, 0.1, and 0.2 S/m (see Figures 4 and 5a). Although the sea ice thicknesses t for station 11 were tightly constrained with $1/f_{MSQ}^- = 0.99$ and $f_{MSQ}^+ = 1.01$ for all three cases, the sea ice conductivities σ showed more variability with $1/f_{MSQ}^-$ and f_{MSQ}^+ varying from 0.92 to 0.99 and from 1.02 to 1.20, respectively. Similar results were found for thicker sea ice (station 31) with $1/f_{MSQ}^-$ between 0.97 and 0.99 and f_{MSQ}^+ between 1.01 and 1.02 for t. The σ showed again more variability with $1/f_{MSQ}^-$ between 0.95 and 0.97 and f_{MSQ}^+ between 1.01 and 1.09. These results were expected because the thickness of a resistive layer is typically better constrained than its conductivity from inductive EM methods (e.g., Pfaffling and Reid, 2009). Similarly, the increase in error with increasing thickness is consistent. The σ is better constrained for higher σ_{syn}, whereas the

most-squares errors of σ are larger for thinner sea ice. Generally, all errors are very low and all parameters are well constrained because only two model parameters are considered.

Experiment 4: Marquardt-Levenberg inversion

To quantify the effect of a priori information, we inverted synthetic data ($\sigma_{syn} = 0.1$ S/m and $t_{syn} = 0 - 10$ m) with different starting models and data weighting.

In a first step, the data set was inverted in a similar manner to experiments 2 and 3. We varied the starting model (Figure 6a) used for each station 3-m-thick sea ice, $\sigma_{syn} = 0.05$ (s1), 0.1 (s2), and 0.2 S/m (s3) and a homogeneous half-space of 2.7 S/m. The starting model did not have a strong influence on sea ice thickness t. The
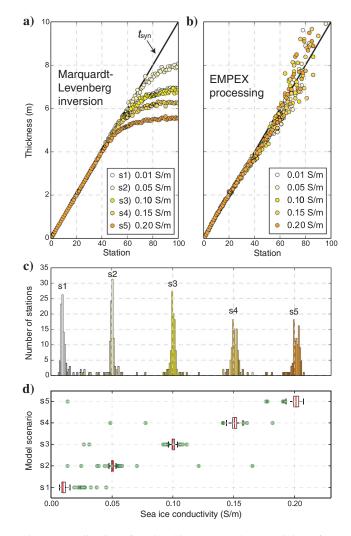

Figure 5. Validation of sea ice thickness t and conductivity σ from (a) Marquardt-Levenberg inversions (experiment 3), and (b) classical single-frequency processing (EMPEX) using the in-phase 5310 Hz component. In panels (a and b), t is compared with t_{syn} of 0–10 m. The Marquardt-Levenberg inversions in panel (a) underestimated t at stations of thick sea ice ($t_{syn} > 5$ m) for all scenarios with σ_{syn} of 0.01 (s1), 0.05 (s2), 0.10 (s3), 0.15 (s4), and 0.20 (s5) S/m. The σ_{syn} is compared to σ obtained from the scenarios s1–s5, illustrated with histograms in panel (c) and box plots in panel (d). Excluding the outliers, σ can be resolved within ± 0.01 S/m, independent from t.

$t_{syn} < 6$ m was reliably reproduced from all conductivities in the starting models (Figure 6a). But even after 300 iterations, the rms error did not reach one (scenarios s1–s3 in Table 2 with rms errors of 1.74–1.87).

In a second step, we used the same starting model as in scenarios s1–s3, but weighted the data misfit according to equation 12. We calculated the weight factors w by using the normalized synthetic data of 5310 Hz in-phase component with added Gaussian noise. Thus, the weight factor w decreased exponentially with increasing station number. Sea ice thickness t (for $t_{syn} > 6$ m) was better resolved compared with the results without weighting (Figure 6b), which was also supported by the reduced rms errors of 0.99–1.16 (scenarios s4–s6 in Table 2). For the starting models with sea ice conductivities of 0.05 and 0.1 S/m, convergence was reached after 104 and 58 iterations, respectively, which was faster than for the other scenarios.

In a third step, we did not weight the data, but we used the sea ice thickness results from the 0.1 S/m exponential fit from Figure 5b in the starting model. In the cases for which it was not possible during EMPEX processing to find for low in-phase values a corresponding sea ice thickness, we used the thickness from the previous station. This is still apparent in the results, in which layered structures are recognizable for sea ice > 9 m (Figure 6c). But t again improved for $t_{syn} > 6$ m compared with the case in Figure 6a. The rms errors of 1.04–1.10 for scenarios s7–s9 were smaller than for scenarios s1–s3 (Table 2). Sea ice thicknesses t from scenarios s7 to s9 were similar and therefore did not depend much on sea ice conductivities of the starting model (Figure 6c).

In general, t was reasonably resolved by the Marquardt-Levenberg algorithm for $t_{syn} < 6$ m, regardless of weights and starting model. With weight factors and results from single-frequency thickness estimates, t improved for $t_{syn} > 6$ m. Although it was not always possible to resolve t up to 10 m, the sea ice conductivities σ were resolved within ± 0.01 S/m for all scenarios (Figure 6d). Outliers of σ rather contained a too-low than a too-high conductivity value.

Porosity estimation

We reformulated Archie's law (Archie, 1942) to calculate the sea ice porosity ϕ

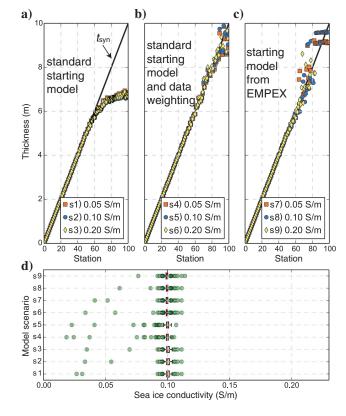$$\phi = \left(\frac{\sigma}{\sigma_b}\right)^{\frac{1}{m}}, \tag{14}$$

Figure 6. Influence of starting model and data weighting on sea ice thickness t and conductivity σ from Marquardt-Levenberg inversions (experiment 4). In comparison with the experiments before, we used here one σ_{syn} of 0.1 S/m, but several starting models that refer to scenarios s1–s9. In panels (a-c), t is compared with t_{syn} of 0–10 m. In panel (a), the standard starting model was used with 3-m-thick sea ice, but variable conductivities of 0.05 (s1), 0.1 (s2), 0.2 (s3) S/m, and an underlying fixed homogeneous half-space of 2.7 S/m. In panel (b), the same starting model was used as in panel (a), but the data were weighted (s4, s5, and s6). In panel (c), sea ice thickness results from EMPEX processing (0.1 S/m in Figure 5b) and sea ice conductivities of 0.05 (s7), 0.1 (s8), 0.2 (s9) S/m were used for the starting model. The t improved with data weighting and a modified starting model obtained from EMPEX thicknesses. In panel (d), σ_{syn} of 0.1 S/m is compared with the resulting sea ice conductivities σ from the individual scenarios, in which σ was recovered for each scenario within ± 0.01 S/m.

Table 1. Error estimates for sea ice conductivities σ and thicknesses t of the two-layer Marquardt-Levenberg models for stations 11 and 31 in Figures 4 and 5a. Error estimates $1/f_{MSQ}^-$ and f_{MSQ}^+ were computed using most-squares inversions involving truncated singular value decomposition with a truncation level $p = 2$, the effective number of model parameters. A model parameter is well-constrained with most-squares errors close to one.

Parameter	$\sigma_{syn} = 0.05$ S/m		$\sigma_{syn} = 0.1$ S/m		$\sigma_{syn} = 0.2$ S/m	
	$1/f_{MSQ}^-$	f_{MSQ}^+	$1/f_{MSQ}^-$	f_{MSQ}^+	$1/f_{MSQ}^-$	f_{MSQ}^+
Station 11						
σ	0.95	1.20	0.92	1.03	0.99	1.02
t	0.99	1.01	0.99	1.01	0.99	1.01
Station 31						
σ	0.97	1.09	0.95	1.02	0.96	1.01
t	0.99	1.02	0.98	1.01	0.97	1.01

where σ is the bulk electrical conductivity, σ_b is the brine conductivity, and m is an empirical cementation factor. Our previous results showed that the uncertainty of σ is 0.01 S/m.

The cementation factor m depends on the connectivity of the pores and the pore shapes, which are related to the structure of sea ice and the c-axis orientation of individual crystals (Reid et al., 2006). The mobility of ions and the permeability are therefore closely linked to this parameter. With respect to sea ice, the literature suggests m between 1.55 and 2.2 (Thyssen et al., 1974; Morey et al., 1984). Haas et al. (1997) and Worby et al. (1999) use a cementation factor of 1.75 for their calculations. Reid et al. (2006) use values of 1.75 and 2.2, stating that the horizontal conductivity of the sea ice is overestimated with a value of 1.75. Because this parameter is not better constrained for sea ice, and also depends on sea ice types and seasonality, we used a value of 1.75.

With temperature measurements of nine first-year sea ice cores from the winter Weddell Sea (Hunkeler et al., 2015), we calculated a mean brine conductivity of 4.69 ± 0.91 S/m according to Stogryn and Desargant (1985). At the same locations, Hunkeler et al. (2015) obtain from EM measurements at 63.03 and 93.09 kHz an average bulk conductivity of 0.06 S/m from seven experiments above thin sea ice (< 1 m). Assuming now $\sigma_b = 4.69 \pm 0.91$ S/m, $m = 1.75$, and $\sigma = 0.06 \pm 0.01$ S/m, we obtain a porosity of $\phi = 8.3 \pm 1.2\%$ using Gaussian law of error propagation. From the nine sea ice cores, we calculated according to Cox and Weeks (1983) and Leppäranta and Manninen (1988) average brine volumes (porosities) of $\phi = 9.5 \pm 5.0\%$. A reasonable sea ice porosity can be estimated from bulk conductivity obtained by EM, according to the agreement between porosities calculated from conductivities and direct measurements in sea ice cores.

DISCUSSION

We have shown that 1D inversions of EM data from passively bucked small coil systems must include the nonlinear contribution of the Bx when working close to a highly conductive environment. In our case of sea ice thickness and conductivity retrieval, the negligence of this contribution would lead to wrong results for sea ice thinner than 2 m (Figure 2b), which is typical of level sea ice thickness in the Arctic and Antarctic landfast sea ice. We calculated synthetic data based on a typical commercial instrument used in sea ice research (Figure 1). The implementation of the bucking bias, however, will need to be made for all frequency-domain EM sensors that use passive bucking in highly conductive environments (Fitterman, 1998). With the effect included, we were able to resolve conduc-

tivity and ultimately porosity with uncertainty values that motivate further studies and use of 1D inversions for field data. This and earlier case studies have shown that, especially, a high-frequency range is required for the retrieval of sea ice conductivity.

Our aim was to jointly resolve sea ice thickness t and conductivity σ for a single layer with a thickness range of t_{syn} of 0–10 m and conductivities σ_{syn} of $0.01 - 0.2$ S/m. We have tested two inversion methods, a smoothness-constrained (EM1DFM) and a Marquardt-Levenberg (EMILIA) inversion. In each scenario, we inverted synthetic data with constant conductivity σ_{syn} and the full range of physically feasible sea ice thicknesses t_{syn}, in which the upper range includes extreme cases, such as decadal sea ice. During each iteration, one single β (trade-off parameter [EM1DFM] or damping factor [EMILIA]) was used for all stations simultaneously. The alternative would be separate inversions of all stations with individual β. This approach may lead to a faster convergence with fewer iterations. However, we chose the single β approach under the assumption that individual stations are not independent to reduce the potential for a wrong minimum of individual inversions.

EM1DFM inverts for the conductivity of multiple fixed layers; therefore, the resolution of thickness depends on how the vertical conductivity gradient is evaluated (Figure 3). The conductivity transition between sea ice and seawater becomes broader for thicker sea ice, and it also depends on σ_{syn}, thus subsequently increasing the uncertainty of the thickness estimate. The Marquardt-Levenberg algorithm instead uses layer thickness and layer conductivity as free parameters, therefore removing the need for retrieving layer interfaces from conductivity gradients (Figure 4). Although the description of sea ice as a layer of defined thickness with a conductivity discontinuity at the ice-water interface is a more realistic description of undeformed sea ice, internal structures such as from sea ice deformation or complex layering potentially can be better described by EM1DFM. However, the uncertainty of the interface location will be increased by the process of vertical conductivity smoothing by EM1DFM. The choice of the inversion scheme therefore depends on the user and the specific application.

The best sea ice thickness results from the Marquardt-Levenberg inversions were found using data weights or tuning the starting model using single-frequency processing results (Figure 6). Higher weights for the weaker signals of thicker sea ice do increase the convergence rate and precision (Table 2). For real field data, we need to be careful when weighting low signal responses because signal noise and instrument attitude errors may have an increased effect. In any case, with both inversion methods, $t_{syn} < 5$ m were reasonably resolved. The conductivities of the starting model

Table 2. Number of iterations and total rms error of scenarios from Figure 6. The starting model contained sea ice conductivities σ_{start} of 0.05, 0.1, or 0.2 S/m. Scenarios s1–s3: starting model with 3 m thick sea ice and underlying homogeneous half-space of 2.7 S/m for all stations. Scenarios s4–s6: same starting model as for scenarios s1–s3, but weighted synthetic data. Scenarios s7–s9: starting model with sea ice thicknesses from single-frequency EMPEX processing.

σ_{start}	Scenarios s1–s3		Scenarios s4–s6		Scenarios s7–s9	
	Rms error	Iterations	Rms error	Iterations	Rms error	Iterations
0.05 S/m	1.74	300	0.99	104	1.04	300
0.1 S/m	1.87	300	0.99	58	1.04	300
0.2 S/m	1.80	300	1.16	300	1.10	300

seemed to have little effect on the inversion results (t_{syn} < 5 m). The constant 3-m-thick starting probably favored the better retrieval of thin sea ice.

Although the sea ice thickness is better constrained than the sea ice conductivity based on the most-squares inversion (Table 1), the conductivity is determined by the Marquardt-Levenberg inversion with the five used frequencies within ±0.01 S/m no matter how well the thickness was resolved, independent of the starting model, the weight factors, and σ_{syn} (Figures 5d and 6d). Likewise, sea ice conductivities can be reasonably well resolved for most of the fixed layers of EM1DFM inversions, provided that the rms error < 2 (Figure 3).

We have simplified sea ice as one homogeneous layer of prescribed thicknesses and conductivities, not accounting for any anisotropy due to higher conductivities in vertical brine channels (Reid et al., 2006). In nature, the simplification of level sea ice most likely applies to thermodynamically grown sea ice, which grows to a maximum of 2.5 m (Thomas and Dieckmann, 2009) or to the Antarctic subice platelet layer with multiple layers of different conductivities (Hunkeler et al., 2015). The sea ice/ocean interface or the interface between sea ice and the platelet layer is characterized by discontinuities in the vertical conductivity structure and by far smaller variability in the horizontal direction. To resolve such structures, we will put effort into improving laterally constrained inversion schemes (Auken et al., 2005). But even such pseudo-2D inversions cannot account for sea ice deformation features, in which conductivities and subice topographies vary additionally on a subfootprint scale. To account for complex topographies of deformed sea ice, we need to include the bucking bias in a full 2D inversion, in which forward-modeling responses and sensitivities are calculated in 2D.

The conversion of conductivity into porosity requires the knowledge of two parameters in Archie's law: (1) the cementation factor and (2) the brine conductivity. First, we assume a cementation factor that is based on the results from previous sea ice field experiments. Second, we used brine conductivities found in Antarctic winter sea ice cores.

For sea ice throughout the freezing season, this parameter is of second-order significance because it is not assumed to vary much. In summer, the brine contains a mixture of saline brine and freshwater due to the surface and internal melting, yielding a higher porosity than winter or spring sea ice (Vancoppenolle et al., 2007; Tison et al., 2008). In such cases, we can still make assumptions about the brine conductivity, but because we deal with higher uncertainties, the effect of porosity and brine conductivity on the bulk sea ice conductivity might not be fully separated in summer cases.

However, the uncertainty range of the sea ice conductivity in this idealized case is promising for retrieving porosity from actual field data. The improvement of 1D sea ice inversions presented in this study therefore has the potential to improve biogeochemical sea ice studies (e.g., Arrigo et al., 1997) and estimations of sea ice density for satellite altimetry retrieval of sea ice thickness (Ricker et al., 2014) by large-scale mapping of sea ice porosity.

CONCLUSION

Sea ice conductivity is a proxy parameter that can be used to derive porosity, albeit systematic measurements on scales larger than point measurements have been rare mostly due to a lack of suitable methodology. With the nondestructive method of multifrequency

EM sounding, this study aims to lay the foundation for an efficient joint retrieval of sea ice thickness and porosity. We varied parameters of a synthetic data set (thickness and conductivity) to assess the sensitivity of different parameter combinations in two geophysical inversion algorithms. Furthermore, we tested the influence of the starting model and data weighting. We calculated the synthetic data for a small-coil system with frequencies relevant for sea ice research in the range of 1–100 kHz. The existing inversion algorithms were modified for a nonlinear correction of signal bias that is caused by passive bucking of the primary EM field close to highly conductive environments. Only with the integration of this sensor-specific correction were we able to determine sea ice conductivity with a resolution of 0.01 S/m with 1D inversion methods. This resolution is sufficient to initiate field trials to estimate sea ice porosity of different sea ice types, the thickness and porosity in multiyear cases, flooded snow layers, or subice platelet layers near Antarctic ice shelves. The detailed knowledge of porosity facilitates biogeochemical studies of sea ice and sea ice densities estimated from porosities yield freeboard validations of satellite measurements. Although our approach improves sea ice surveying with EM induction sounding methods, it suffers the same limitations caused by the use of 1D forward models for essentially 3D targets with a significant subfootprint-scale variability. Because real-world sea ice surveys are mostly conducted along transects, we suggest modifying 2D inversions methods to resolve thickness and internal conductivity changes at subfootprint scales. Such a method would enable further studies of sea ice deformation, relevant for the improved estimation of sea ice volume.

ACKNOWLEDGMENTS

REFERENCES

Anderson, W. L., 1979, Numerical integration of related Hankel transforms of orders 0 and 1 by adaptive digital filtering: Geophysics, **44**, 1287–1305, doi: 10.1190/1.1441007.

Archie, G. E., 1942, The electrical resistivity log as an aid in determining some reservoir characteristics: Transactions of the AIME, **146**, 54–62, doi: 10.2118/942054-G.

Arrigo, K. R., D. L. Worthen, M. P. Lizotte, P. Dixon, and G. Dieckmann, 1997, Primary production in Antarctic sea ice: Science, **276**, 394–397, doi: 10.1126/science.276.5311.394.

Auken, E., A. V. Christiansen, B. H. Jacobsen, N. Foged, and K. I. Sørensen, 2005, Piecewise 1D laterally constrained inversion of resistivity data: Geophysical Prospecting, **53**, 497–506, doi: 10.1111/j.1365-2478.2005.00486.x.

Comiso, J. C., and D. K. Hall, 2014, Climate trends in the Arctic as observed from space: Wiley Interdisciplinary Reviews: Climate Change, **5**, 389–409, doi: 10.1002/wcc.277.

Cox, G. F. N., and W. F. Weeks, 1983, Equations for determining the gas and brine volumes in sea ice samples: Journal of Glaciology, **29**, 306–316.

Druckenmiller, M. L., H. Eicken, M. A. Johnson, D. J. Pringle, and C. C. Williams, 2009, Toward an integrated coastal sea-ice observatory: System components and a case study at Barrow, Alaska: Cold Regions Science and Technology, **56**, 61–72, doi: 10.1016/j.coldregions.2008.12.003.

Eicken, H., H. R. Krouse, D. Kadko, and D. K. Perovich, 2002, Tracer studies of pathways and rates of meltwater transport through Arctic summer sea ice: Journal of Geophysical Research: Oceans, **107**, SHE 22-1–SHE 22-20, doi: 10.1029/2000JC000583.

Eicken, H., W. Tucker, and D. Perovich, 2001, Indirect measurements of the mass balance of summer Arctic sea ice with an electromagnetic induction technique: Annals of Glaciology, **33**, 194–200, doi: 10.3189/172756401781818356.

Farquharson, C., 2000, Background for Program EM1DFM: University of British Columbia.

Farquharson, C., and D. Oldenburg, 1993, Inversion of time-domain electromagnetic data for a horizontally layered Earth: Geophysical Journal International, **114**, 433–442, doi: 10.1111/j.1365-246X.1993.tb06977.x.

Farquharson, C., and D. Oldenburg, 1996, Approximate sensitivities for the electromagnetic inverse problem: Geophysical Journal International, **126**, 235–252, doi: 10.1111/j.1365-246X.1996.tb05282.x.

Farquharson, C. G., D. W. Oldenburg, and P. S. Routh, 2003, Simultaneous 1D inversion of loop-loop electromagnetic data for magnetic susceptibility and electrical conductivity: Geophysics, **68**, 1857–1869, doi: 10.1190/1.1635038.

Fitterman, D. V., 1998, Sources of calibration errors in helicopter EM data: Exploration Geophysics, **29**, 65–70, doi: 10.1071/EG998065.

Gill, P. E., W. Murray, and M. H. Wright, 1981, Practical optimization: Academic Press.

Golden, K., H. Eicken, A. Heaton, J. Miner, D. Pringle, and J. Zhu, 2007, Thermal evolution of permeability and microstructure in sea ice: Geophysical Research Letters, **34**, L16501, doi: 10.1029/2007GL030447.

Gosink, T. A., J. G. Pearson, and J. J. Kelley, 1976, Gas movement through sea ice: Nature, **263**, 41–42, doi: 10.1038/263041a0.

Grab, M., 2012, Forward and inverse modelling of frequency-domain electromagnetic data from small coils: Master's thesis, IDEA League, ETH Zurich.

Haas, C., 1998, Evaluation of ship-based electromagnetic-inductive thickness measurements of summer sea-ice in the Bellingshausen and Amundsen Seas, Antarctica: Cold Regions Science and Technology, **27**, 1–16, doi: 10.1016/S0165-232X(97)00019-0.

Haas, C., 2004, Late-summer sea ice thickness variability in the Arctic Transpolar Drift 19912001 derived from ground-based electromagnetic sounding: Geophysical Research Letters, **31**, L09402, doi: 10.1029/2003GL019394.

Haas, C., S. Gerland, H. Eicken, and H. Miller, 1997, Comparison of sea-ice thickness measurements under summer and winter conditions in the Arctic using a small electromagnetic induction device: Geophysics, **62**, 749–757, doi: 10.1190/1.1444184.

Haas, C., S. Hendricks, H. Eicken, and A. Herber, 2010, Synoptic airborne thickness surveys reveal state of Arctic sea ice cover: Geophysical Research Letters, **37**, L09501, doi: 10.1029/2010GL042652.

Haas, C., J. Lobach, S. Hendricks, L. Rabenstein, and A. Pfaffling, 2009, Helicopter-borne measurements of sea ice thickness, using a small and lightweight, digital EM system: Journal of Applied Geophysics, **67**, 234–241, doi: 10.1016/j.jappgeo.2008.05.005.

Haas, C., A. Pfaffling, S. Hendricks, L. Rabenstein, J. Etienne, and I. Rigor, 2008, Reduced ice thickness in Arctic Transpolar Drift favors rapid ice retreat: Geophysical Research Letters, **35**, L17501, doi: 10.1029/2008GL034457.

Holladay, J. S., R. Z. Moucha, and S. J. Prinsenberg, 1998, Airborne electromagnetic sea ice sounding measurements during SIMMS'95: Canadian Contractor Report of Hydrography and Ocean Sciences 50.

Hoppmann, M., M. Nicolaus, S. Paul, P. A. Hunkeler, G. Heinemann, S. Willmes, R. Timmermann, O. Boebel, T. Schmidt, M. Kiihnel, G. Konig-Langlo, and R. Gerdes, 2015, Ice platelets below Weddell Sea landfast sea ice: Annals of Glaciology, **56**, 175–190, doi: 10.3189/2015AoG69A678.

Hunkeler, P. A., S. Hendricks, M. Hoppmann, S. Paul, and R. Gerdes, 2015, Towards an estimation of sub sea-ice platelet-layer volume with multi-frequency electromagnetic induction sounding: Annals of Glaciology, **56**, 137–146, doi: 10.3189/2015AoG69A705.

Jackson, D. D., 1976, Most squares inversion: Journal of Geophysical Research, **81**, 1027–1030, doi: 10.1029/JB081i005p01027.

Jupp, D., and K. Vozoff, 1975, Stable iterative methods for the inversion of geophysical data: Geophysical Journal International, **42**, 957–976, doi: 10.1111/j.1365-246X.1975.tb06461.x.

Kalscheuer, T., M. Bastani, S. Donohue, L. Persson, A. Pfaffhuber, F. Reiser, and Z. Ren, 2013, Delineation of a quick clay zone at Smørgrav, Norway, with electromagnetic methods under geotechnical constraints: Journal of Applied Geophysics, **92**, 121–136, doi: 10.1016/j.jappgeo.2013.02.006.

Kalscheuer, T., J. Hübert, A. Kuvshinov, T. Lochbiihler, and L. B. Pedersen, 2012, A hybrid regularization scheme for the inversion of magnetotelluric data from natural and controlled sources to layer and distortion parameters: Geophysics, **77**, no. 4, E301–E315, doi: 10.1190/geo2012-0018.1.

Kalscheuer, T., M. D. l. Á. G. Juanatey, N. Meqbel, and L. B. Pedersen, 2010, Non-linear model error and resolution properties from two-dimensional single and joint inversions of direct current resistivity and radiomagnetotelluric data: Geophysical Journal International, **182**, 1174–1188, doi: 10.1111/j.1365-246X.2010.04686.x.

Kalscheuer, T., and L. B. Pedersen, 2007, A non-linear truncated SVD variance and resolution analysis of two-dimensional magnetotelluric models: Geophysical Journal International, **169**, 435–447, doi: 10.1111/j.1365-246X.2006.03320.x.

Kaufmann, M., 2014, Pseudo 2D inversion of multi-frequency coil-coil FDEM data: Master's thesis, IDEA League, ETH Zurich.

Kovacs, A., 1996, Sea ice: Part II. Estimating the full-scale tensile, flexural, and compressive strength of first-year ice, Technical report, Defense Technical Information Center Document.

Kovacs, A., and J. S. Holladay, 1990, Sea-ice thickness measurement using a small airborne electromagnetic sounding system: Geophysics, **55**, 1327–1337, doi: 10.1190/1.1442780.

Kovacs, A., J. S. Holladay, and C. J. Bergeron Jr., 1995, The footprint/altitude ratio for helicopter electromagnetic sounding of sea-ice thickness: Comparison of theoretical and field estimates: Geophysics, **60**, 374–380, doi: 10.1190/1.1443773.

Kovacs, A., and R. M. Morey, 1991, Sounding sea ice thickness using a portable electromagnetic induction instrument: Geophysics, **56**, 1992–1998, doi: 10.1190/1.1443011.

Krembs, C., H. Eicken, and J. W. Deming, 2011, Exopolymer alteration of physical properties of sea ice and implications for ice habitability and biogeochemistry in a warmer Arctic: Proceedings of the National Academy of Sciences, **108**, 3653–3658, doi: 10.1073/pnas.1100701108.

Kwok, R., G. F. Cunningham, M. Wensnahan, I. Rigor, H. J. Zwally, and D. Yi, 2009, Thinning and volume loss of the Arctic Ocean sea ice cover: 2003–2008: Journal of Geophysical Research, **114**, C07005, doi: 10.1029/2009JC005312.

Langhorne, P. J., K. Hughes, A. J. Gough, I. J. Smith, M. Williams, N. Robinson, C. Stevens, W. Rack, D. Price, G. Leonard, A. Mahoney, C. Haas, and T. Haskell, 2015, Observed platelet ice distributions in antarctic sea ice: An index for ocean — Ice shelf heat flux: Geophysical Research Letters. **42**, 5442–5451, doi: 10.1002/2015GL064508.

Leppäranta, M., and T. Manninen, 1988, The brine and gas content of sea ice with attention to low salinities and high temperatures, Finnish Institute of Marine Research, internal report, 1988–2.

Lindsay, R., and J. Zhang, 2005, The thinning of Arctic sea ice, 1988-2003: Have we passed a tipping point?: Journal of Climate, **18**, 4879–4894, doi: 10.1175/JCLI3587.1.

Lines, L., and S. Treitel, 1984, Tutorial: A review of least-squares inversion and its application to geophysical problems: Geophysical Prospecting, **32**, 159–186, doi: 10.1111/j.1365-2478.1984.tb00726.x.

Maslanik, J., J. Stroeve, C. Fowler, and W. Emery, 2011, Distribution and trends in Arctic sea ice age through spring 2011: Geophysical Research Letters, **38**, L13502, doi: 10.1029/2011GL047735.

Meju, M., and V. Hutton, 1992, Iterative most-squares inversion: Application to magnetotelluric data: Geophysical Journal International, **108**, 758–766, doi: 10.1111/j.1365-246X.1992.tb03467.x.

Meju, M. A., 1994, Biased estimation: A simple framework for inversion and uncertainty analysis with prior information: Geophysical Journal International, **119**, 521–528, doi: 10.1111/j.1365-246X.1994.tb00139.x.

Menke, W., 1989, Geophysical data analysis: Discrete inverse theory: Academic Press, International Geophysics Series 45.

Morey, R. M., A. Kovacs, and G. F. Cox, 1984, Electromagnetic properties of sea ice: Cold Regions Science and Technology, **9**, 53–75, doi: 10.1016/0165-232X(84)90048-X.

Nicolaus, M., C. Katlein, J. Maslanik, and S. Hendricks, 2012, Changes in Arctic sea ice result in increasing light transmittance and absorption: Geophysical Research Letters, **39**, L24501, doi: 10.1029/2012GL053738.

Niedrauer, T. M., and S. Martin, 1979, An experimental study of brine drainage and convection in young sea ice: Journal of Geophysical Research: Oceans, **84**, 1176–1186, doi: 10.1029/JC084iC03p01176.

Notz, D., and M. G. Worster, 2008, In situ measurements of the evolution of young sea ice: Journal of Geophysical Research: Oceans, **113**, C03001, doi: 10.1029/2007JC004333.

Paige, C. C., and M. A. Saunders, 1982, LSQR: An algorithm for sparse linear equations and sparse least squares: ACM Transactions on Mathematical Software (TOMS), **8**, 43–71, doi: 10.1145/355984.355989.

Perovich, D., K. Jones, B. Light, H. Eicken, T. Markus, J. Stroeve, and R. Lindsay, 2011, Solar partitioning in a changing Arctic sea-ice cover: Annals of Glaciology, **52**, 192–196, doi: 10.3189/172756411795931543.

Pfaffhuber, A. A., S. Hendricks, and Y. A. Kvistedal, 2012, Progressing from 1D to 2D and 3D near-surface airborne electromagnetic mapping with a multisensor, airborne sea-ice explorer: Geophysics, **77**, no. 4, WB109–WB117, doi: 10.1190/geo2011-0375.1.

Pfaffling, A., C. Haas, and J. E. Reid, 2007, A direct helicopter EM sea ice thickness inversion, assessed with synthetic and field data: Geophysics, **72**, no. 4, F127–F137, doi: 10.1190/1.2732551.

Pfaffling, A., and J. E. Reid, 2009, Sea ice as an evaluation target for HEM modelling and inversion: Journal of Applied Geophysics, **67**, 242–249, doi: 10.1016/j.jappgeo.2008.05.010.

Pringle, D., J. Miner, H. Eicken, and K. Golden, 2009, Pore space percolation in sea ice single crystals: Journal of Geophysical Research: Oceans, **114**, C12017, doi: 10.1029/2008JC005145.

Rack, W., C. Haas, and P. J. Langhorne, 2013, Airborne thickness and freeboard measurements over the McMurdo Ice Shelf, Antarctica, and implications for ice density: Journal of Geophysical Research: Oceans, **118**, 5899–5907, doi: 10.1002/2013JC009084.

Reid, J. E., A. Pfaffling, A. P. Worby, and J. R. Bishop, 2006, In situ measurements of the direct-current conductivity of Antarctic sea ice: Implications for airborne electromagnetic sounding of sea-ice thickness: Annals of Glaciology, **44**, 217–223, doi: 10.3189/172756406781811772.

Reid, J. E., A. P. Worby, J. Vrbancich, and A. I. S. Munro, 2003, Shipborne electromagnetic measurements of Antarctic sea-ice thickness: Geophysics, **68**, 1537–1546, doi: 10.1190/1.1620627.

Ricker, R., S. Hendricks, V. Helm, H. Skourup, and M. Davidson, 2014, Sensitivity of CryoSat-2 Arctic sea-ice freeboard and thickness on radar-waveform interpretation: The Cryosphere, **8**, 1607–1622, doi: 10.5194/tc-8-1607-2014.

Spies, B. R., and F. C. Frischknecht, 1991, Electromagnetic sounding, *in* M. N. Nabighian, ed., Electromagnetic methods in applied geophysics: Volume 2, application, Parts A and B: SEG Investigations in Geophysics No. 3, 285–425.

Stogryn, A., and G. Desargant, 1985, The dielectric properties of brine in sea ice at microwave frequencies: IEEE Transactions on Antennas and Propagation, **33**, 523–532, doi: 10.1109/TAP.1985.1143610.

Stroeve, J. C., M. C. Serreze, M. M. Holland, J. E. Kay, J. Malanik, and A. P. Barrett, 2012, The Arctics rapidly shrinking sea ice cover: A research synthesis: Climatic Change, **110**, 1005–1027, doi: 10.1007/s10584-011-0101-1.

Thomas, D. N., and G. S. Dieckmann, 2009, Sea ice: John Wiley & Sons.

Thyssen, F., H. Kohnen, M. Cowan, and G. Timco, 1974, DC resistivity measurements on the sea ice near pond inlet, NWT (Baffin Island): Polarforschung, **44**, 117–126.

Tison, J.-L., A. Worby, B. Delille, F. Brabant, S. Papadimitriou, D. Thomas, J. De Jong, D. Lannuzel, and C. Haas, 2008, Temporal evolution of decaying summer first-year sea ice in the Western Weddell Sea, Antarctica: Deep Sea Research Part II Topical Studies in Oceanography, **55**, 975–987, doi: 10.1016/j.dsr2.2007.12.021.

Vancoppenolle, M., C. M. Bitz, and T. Fichefet, 2007, Summer landfast sea ice desalination at Point Barrow, Alaska: Modeling and observations: Journal of Geophysical Research: Oceans, **112**, C04022, doi: 10.1029/2006JC003493.

Vancoppenolle, M., H. Goosse, A. De Montety, T. Fichefet, B. Tremblay, and J.-L. Tison, 2010, Modeling brine and nutrient dynamics in Antarctic sea ice: The case of dissolved silica: Journal of Geophysical Research: Oceans, **115**, C02005, doi: 10.1029/2009JC005369.

Weissling, B., M. Lewis, and S. Ackley, 2011, Sea-ice thickness and mass at ice station Belgica, Bellingshausen Sea, Antarctica: Deep Sea Research Part II: Topical Studies in Oceanography, **58**, 1112–1124, doi: 10.1016/j.dsr2.2010.10.032.

Won, I. J., A. Oren, and F. Funak, 2003, GEM-2A: A programmable broadband helicopter-towed electromagnetic sensor: Geophysics, **68**, 1888–1895, doi: 10.1190/1.1635041.

Worby, A., P. Griffin, V. Lytle, and R. Massom, 1999, On the use of electromagnetic induction sounding to determine winter and spring sea ice thickness in the Antarctic: Cold Regions Science and Technology, **29**, 49–58, doi: 10.1016/S0165-232X(99)00003-8.